Atmospheric gravity wave impacts on an offshore wind farm

S J Ollier, S.J.; Watson, S. J.; Montavon, C

Important note
To cite this publication, please use the final published version (if applicable).
Please check the document version above.

PAPER • OPEN ACCESS

Atmospheric gravity wave impacts on an offshore wind farm

View the article online for updates and enhancements.
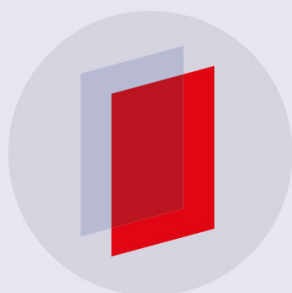
IOP **ebooks**™

Bringing you innovative digital publishing with leading voices to create your essential collection of books in STEM research.

Start exploring the collection - download the first chapter of every title for free.

Atmospheric gravity wave impacts on an offshore wind farm

S J Ollier[1], S J Watson[1,2], C Montavon[3]

[1]CREST – Loughborough University, Holywell Park, Loughborough LE11 3TU, UK
[2]DUWIND – Delft University of Technology, Kluyverweg 1, 2629 HS Delft, Netherlands.
[3]Independent Researcher, H. Marsmanplantsoen 11, 2548 EJ 's-Gravenhage, The Netherlands

Abstract. Atmospheric Gravity Waves (AGWs) frequently occur around near coastal offshore wind farms. Yet our understanding of how they interact with individual turbines and whole farm energy output is limited. This research uses computational fluid dynamics modelling to investigate the impact of near coastal, topographically forced AGWs on offshore wind farm power output in a theoretical wind farm. Preliminary results show the farm contained within one wavelength (4.9km) of the topographically forced AGW. The AGW causes a substantial variation in wind speed across the farm with a subsequent 76% variation in power output compared to 29% in the control case.

1.Introduction
Atmospheric Gravity Waves (AGWs) often result from displacement of flow by topographical obstacles in neutral or stable surface atmospheric conditions with a strong temperature inversion above the atmospheric boundary layer. They also form via jet stream turbulence, weather fronts, cold air outbreaks, thunderstorms, tornadoes, hurricanes, polar lows and other unknown sources [1–5]. AGWs are frequent in the offshore environment and influence marine atmospheric boundary layer wind fields over large areas of the ocean, e.g. [7,8]. Stability effects aloft, which are often introduced by the changes in roughness and temperature at coast-sea transition, lead to an oscillation of this displaced flow, creating waves.

Whilst [9–11] investigate the propagation of AGWs by wind farms, to our knowledge. no one has investigated the influence of pre-existing AGWs on individual turbines or whole wind farms, on or offshore. Considering their influence on offshore wind fields, AGWs are likely to be important for offshore wind power. Thus, this research investigates the influence of AGWs on offshore wind farm power output. We use a theoretical offshore wind farm downstream of a topographical obstacle to simulate the impact of AGWs on the wind energy output.

2.Methodology
We use two CFD simulations, a control case and an AGW case, to demonstrate the impact of AGWs on the conditions reaching the turbines and the subsequent power output. The simulations use the same domain set up (section 2.1) and wind farm layout (section 2.3) but differing topographies (section 2.2) and boundary conditions (section 2.4). The control and AGW cases are based on the same prevailing upstream conditions and thus demonstrate the differences in flow in response to conditions that favour AGW propagation.

CFD simulations are run with ANSYS Windmodeller [12] using the CFX Solver. The model solves the Reynolds Averaged Navier Stokes (RANS) equations with a k -ε turbulence model with a modified set of constants (coefficient of eddy viscosity, Cμ = 0.03, turbulence decay rate = 0.6, section 2.4) as previously validated in [17]. Atmospheric stability is modeled by solving a transport equation for the dry potential temperature, accounting for buoyancy effects in the vertical momentum equation as well as in the turbulence model [15]. To isolate the AGW effects on the wind farm, Coriolis effects are not included in these initial simulations.

2.1. Domain set-up

We use a cuboid domain with 32km length, 20km width and 10km height (Figure 1). The height of the domain was chosen to avoid unphysical numerical reflections of the gravity waves. The background horizontal resolution (outside of the rotor regions) for the model domain is 60m. In the vertical, the mesh resolution follows a geometric progression with 68 levels where the first cell above the ground has a thickness of 2m and the geometric expansion factor is 1.09. There is a more refined mesh in the vicinity of the turbine rotors, where the mesh adaption algorithm results in a mesh with approximately 15 cells vertically across the rotors.

2.2. Topography

For the AGW case, the topography is a simplified representation of a typical near coastal hill in the UK. We introduce a simple coastal ridge based on a 2-dimensional 'Witch of Agnesi', where hill height $h(x)$ relates to the maximum hill height (h_m , 275m) and hill half-width (a , 276m):

$$h(x) = \frac{h_m . a^2}{x^2 + a^2} \qquad (1)$$

This 2-dimensional hill is elongated to form a ridge aligned perpendicular to the incoming wind, which blows along the x-direction (Figure 1). The surface roughness of the ridge and coastline are both 0.03m, the rest of the domain is ocean with a roughness length of 0.0002m. The control domain does not include topography and has a constant surface roughness of 0.03m.
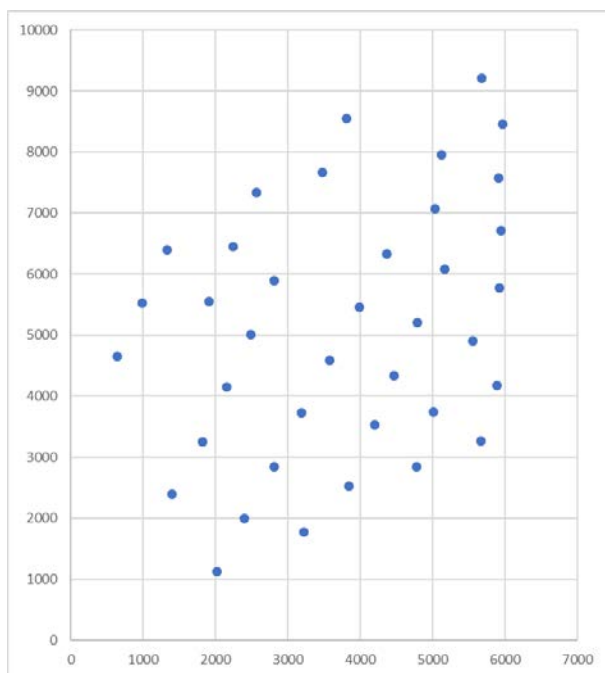
Figure 1. Wind farm layout with coordinates in metres.
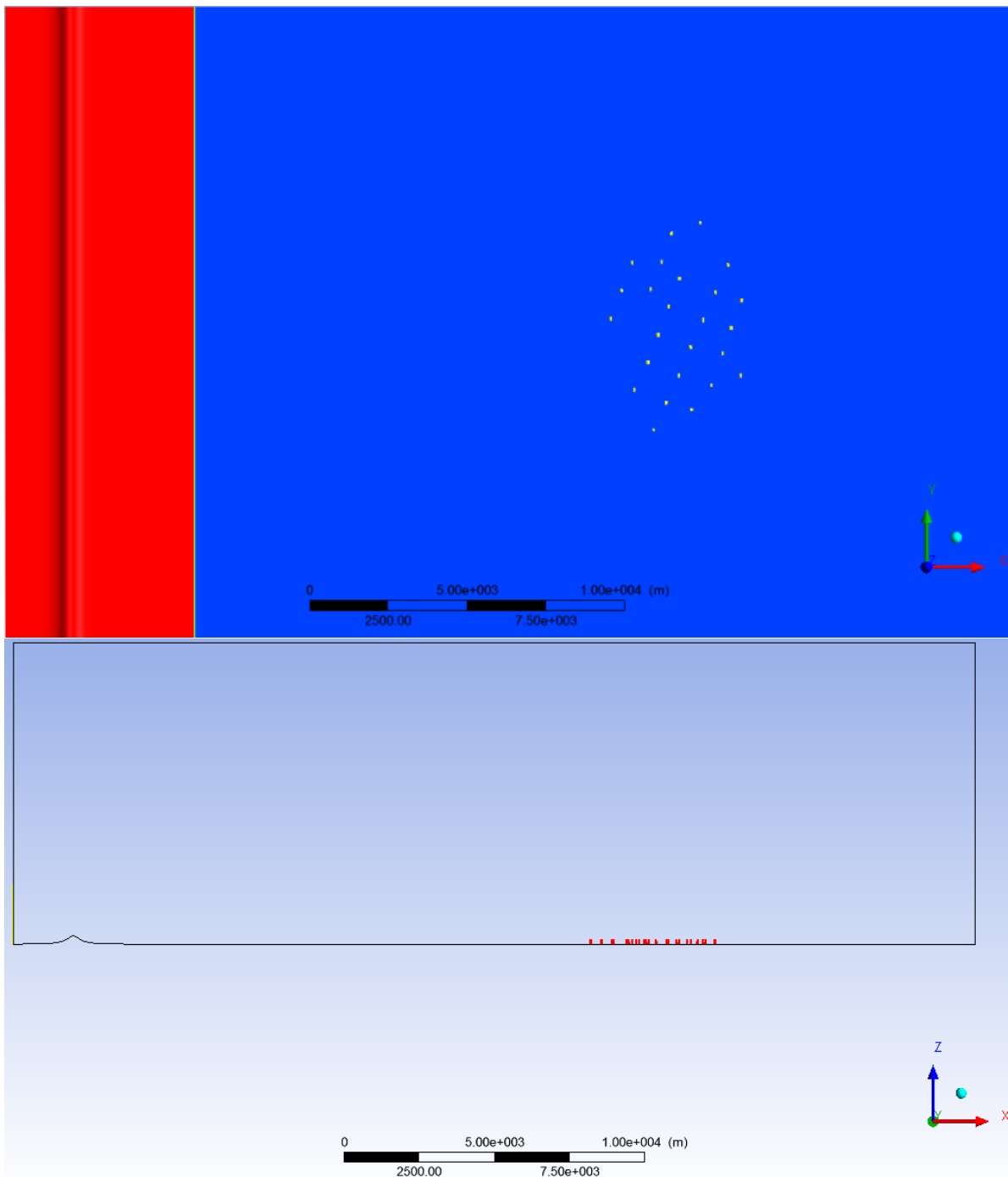
Figure 2. Top: view from above of model domain. Red areas are land, and blue are offshore, the grey line represents the ridge and each yellow dot cross represents a single turbine location. Bottom: side view with the coastal ridge at the inlet, each red dot represents a single wind turbine. Scale bar at the bottom of each image.

2.3. Wind Farm

The wind farm is 15km offshore and contains 25 Siemens SWT36-107 turbines with 77m hub heights and rotor diameters of 10 m with a layout as shown in Figure 1. The cut-in wind speed for these turbines is 3 -5ms^{-1}, rated wind speed is 13-14ms^{-1} and cut-out speed is 25ms^{-1}. For a realistic turbine array, the

wind farm layout is based on a subset of the existing offshore wind farm Greater Gabbard, from the Northern section of the farm layout. This is 2.6km long, 3.8km wide (Figure 2).

Turbine power output is based on the SWT36-107 Power curve [13]. Wake effects were accounted for by an actuator disk model in Windmodeller using thrust data for the SWT36-107 turbine. The upstream wind speeds for individual turbines are also calculated using actuator disk theory. The upflow angle α at the hub location has been calculated from the vertical velocity, V_z, and the horizontal velocity, V_h, as follows:

$$\alpha = \text{atan}\left(\frac{V_z}{V_h}\right) \tag{2}$$

$$V_h = \sqrt{V_x^2 + V_y^2} \tag{3}$$

where V_x and V_y are the velocity vectors in the x- and y-direction respectively.

2.4. Boundary conditions

At the inlet (Western plane), Dirichlet boundary conditions (i.e., prescribed profiles) are applied for the velocity vector, the potential temperature θ and the turbulence quantities (turbulence kinetic energy k and turbulence dissipation rate ε). For the pressure, a zero-gradient condition is applied. The inlet profiles for the relevant variables were set up as follows: below the boundary layer height, h_{BL}, the velocity profile follows a log profile, while above it the profile is bounded to the velocity value at the top of the boundary layer, V_G. With the flow directed along the x-axis, we have the following velocity profiles for the velocity components:

$$V_x(z) = min\left(\frac{u_*}{\kappa} ln\left(\frac{z}{z_{0,upstream}}\right), V_G\right) \tag{4}$$

$$V_y = V_z = 0 \tag{5}$$

In the case set up here, we assumed an upstream roughness ($z_{0,upstream}$) of 0.03m and set the profile by calculating u_* so thatwe have a reference wind speed of 8 m/s at a reference height of 70m. κ is the von Karman constant, set at a value of 0.41 in ANSYS CFX. The boundary layer height is calculated from the empirical relationship [14]:

$$h_{BL} = 0.25\frac{u_*}{f} \tag{6}$$

with f the Coriolis parameter (set to a value of $1.2 \ 10^{-4} \ s^{-1}$ in the simulation as representative for mid-latitudes). The inlet profiles for the turbulence kinetic energy and dissipation rate are set with:

$$k(z) = max\left[\frac{u_*^2}{\sqrt{C_\mu}}\left(1 - \frac{z}{h_{BL}}\right)^{1.68}, 10^{-4} \ m^2/s^2\right] \tag{7}$$

$$\varepsilon(z) = max\left[\frac{u_*^3}{\kappa z} 1.03 \ F_{cor} \ exp\left(-2.8\left(\frac{z}{h_{BL}}\right)^2\right), 10^{-4} \ m^2/s^3\right] \tag{8}$$

$$F_{cor} = \left[1 + \frac{0.015}{z^{0.9}} max\left(0, ln\frac{z}{z_0}\right)\right] \tag{9}$$

where F_{cor} is a roughness dependent correction factor. The profiles for the turbulence quantities in equations (7) and (8) are empirically based on numerical results obtained for a 1D simulation of a developing boundary layer over the sea, after 24 hours of physical time [15].

   The control case did not include atmospheric stability, with a fixed temperature of 288 K throughout the domain. Note that an alternative control could be an identical set-up as for the test case but with no hill, however, the roughness change also produces AGWs albeit of a lower magnitude. Also, the turbines themselves will induce small gravity waves. As our aim was to compare an AGW case with a non-AGW case, it was felt that the chosen control was more appropriate. In addition, as the surface layer was neutral in both cases, wake losses will be similar as for the AGW case. Further work will be required to compare with a range of control cases.

For the AGW case, the inflow profile for the potential temperature, (θ), assumes a well-mixed neutral boundary layer, capped by an inversion layer with height, z_{inv}, between 900m and 1000m, with strongly stable conditions in the inversion layer. The height of the inversion layer is approximately that given by Eq. (6) for the reference wind speed and mid-latitude chosen. Above this capping inversion, the atmosphere is stable with the potential temperature gradient of the standard atmosphere (3.3 K/km). The potential temperature profile is given in three sections with:

$$\theta = \theta_1 \qquad\qquad z < z_{inv} - d \qquad\qquad (10)$$

$$\theta = \theta_1 + (\partial\theta/\partial z)_{inv}[z - (z_{inv} - d)] \qquad\qquad z_{inv} - d < z < z_{inv}$$

$$\theta = \theta_0 + (\partial\theta/\partial z)_0 z \qquad\qquad z > z_{inv}$$

$(\partial\theta/\partial z)_0$ the freestream potential temperature gradient was set to 3.3 x 10^{-3} [K/m] in line with the International Standard Atmosphere (ISO 2533:1975). The potential temperature gradient in the inversion is calculated as $(\partial\theta/\partial z)_{inv} = (\theta_0 + (\partial\theta/\partial z)_0 z_{inv} - \theta_1)/d$. The profile schematic is shown in (Figure 3). For the case simulated, the top of the inversion height z_{inv} was set to 1000m, and the inversion thickness d was 100m. The reference potential temperature θ_0 was 294K and the potential temperature in the boundary layer at the inflow, θ_1, was 288K, giving a temperature difference of 9.3K across the inversion.
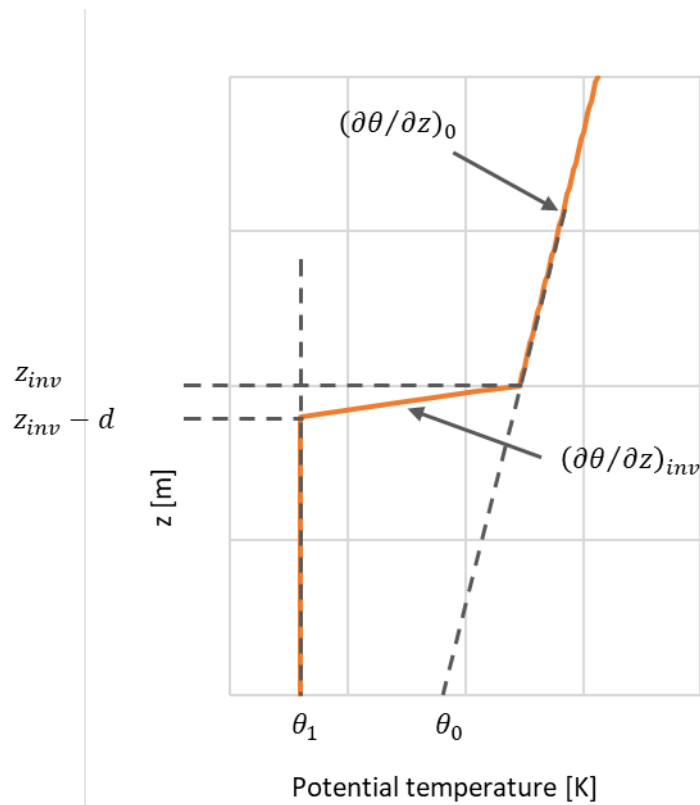
Figure 3. Schematic of potential temperature profile applied at the inflow.

At the outlet (Eastern plane) and at the top of the domain, an entrainment opening boundary condition is used which applies:

- zero-gradient condition on the velocity
- zero-gradient on the potential temperature and turbulence quantities when the flow is locally out of the domain. If the flow is entering the domain at those locations, the model then applies the same prescribed profiles as those used for the inflow.
- A Dirichlet boundary condition for the pressure, where the prescribed pressure profile is calculated to satisfy the hydrostatic balance associated with the potential temperature profile applied at the inflow.[1]

At the sides of the domain (Northern and Southern planes), symmetry conditions are used for all variables. At the ground, no-slip boundary conditions are used for the velocity, using wall functions to characterize the momentum fluxes as a function of the local roughness and friction velocity u_τ , where $u_\tau = C_\mu^{1/4} k^{1/2}$ [16]. Adiabatic (i.e., zero flux) conditions are used for the potential temperature (implying neutral surface stability conditions) and for the turbulence kinetic energy. The closure for the turbulence dissipation rate at the ground is provided by the algebraic relationship:

---

[1] When no flow prevails in the domain, the momentum conservation equation in the vertical is simplified to $\frac{\partial p}{\partial z} = g\rho \frac{1}{\theta_0}(\theta - \theta_0)$. The pressure profile used at the outflow is calculated by integrating this relationship from the ground to the top of the domain, using the prescribed profile for θ at the inflow, and the reference potential temperature θ_0. When using a pressure profile not satisfying the hydrostatic balance, the model generates flow acceleration or slow-down that can destabilise the solution. g is gravitational acceleration and ρ is air density.

$$\varepsilon = \frac{u_\tau^3}{\kappa z}$$

(11)

a closure consistent with the neutral surface layer specification.

3.Preliminary results

In the AGW case, standing AGWs form in the model domain with 4.9km wavelength and oscillate through the wind farm (Figure 4, Figure 5) compared with the control where no AGWs are present (Figure 5). Whilst all turbines except those on the western edge are subject to wake effects, the influence of the AGW is still apparent in both the wind speed and the power output (Figure 5). With the same inlet wind speed (8 ms^{-1}) the wind speeds directly upstream of the turbines deviate dramatically between the control and AGW cases (upstream U, Table 1, Figure 6).

As the turbines are spaced across a cycle of the AGW, the wind speeds experienced by the individual turbines across the farm varied by up to 4.3ms $^{-1}$ (6.7ms $^{-1}$ – 11.0ms $^{-1}$ with a standard deviation of 1.3ms^{-1}). The highest wind speeds are along the western and eastern edges, with a dip in the centre of the AGW minimum. Whilst all turbines experience above cut-in windspeeds, these variations result in a substantial drop-off in power output towards the centre of the farm at the lower wind speed region of the AGW (Figure 4, Figure 5, Figure 6) giving a minimum turbine power of 743kW, 76 % lower than the maximum at the far eastern edge (3063kW). This is compared to a 29% (1413kW- 1002kW) variation in power across the wind farm in the control case (Table 1).

The total output for the farm is 42448kW (standard deviation (s.d.) 718kW) compared with 31662kW (s.d. 122kW) for the control, whilst the range of power is 2320kW versus 411kW (s.d. 718kW), respectively. The upflow angle was also considerably more variable in the AGW case (standard deviation 0.09^{o}) versus the control case (Table 1, Figure 6)

Table 1. Power, upflow angle and upstream windspeed for the turbines in the Control and AGW runs.

	AGW					Control				
	Max	min	mean	s.d.	total power	max	min	Mean	s.d.	total power
Power (kW)	3062.86	742.96	1697.91	718.33	42447.64	1413.48	1002.02	1266.47	122.02	31661.86
α (º)	2.70	-1.06	0.89	1.10		1.44	0.52	0.98	0.26	
upstream U (ms^{-1})	11.04	6.75	8.73	1.28		8.32	7.43	8.03	0.27	
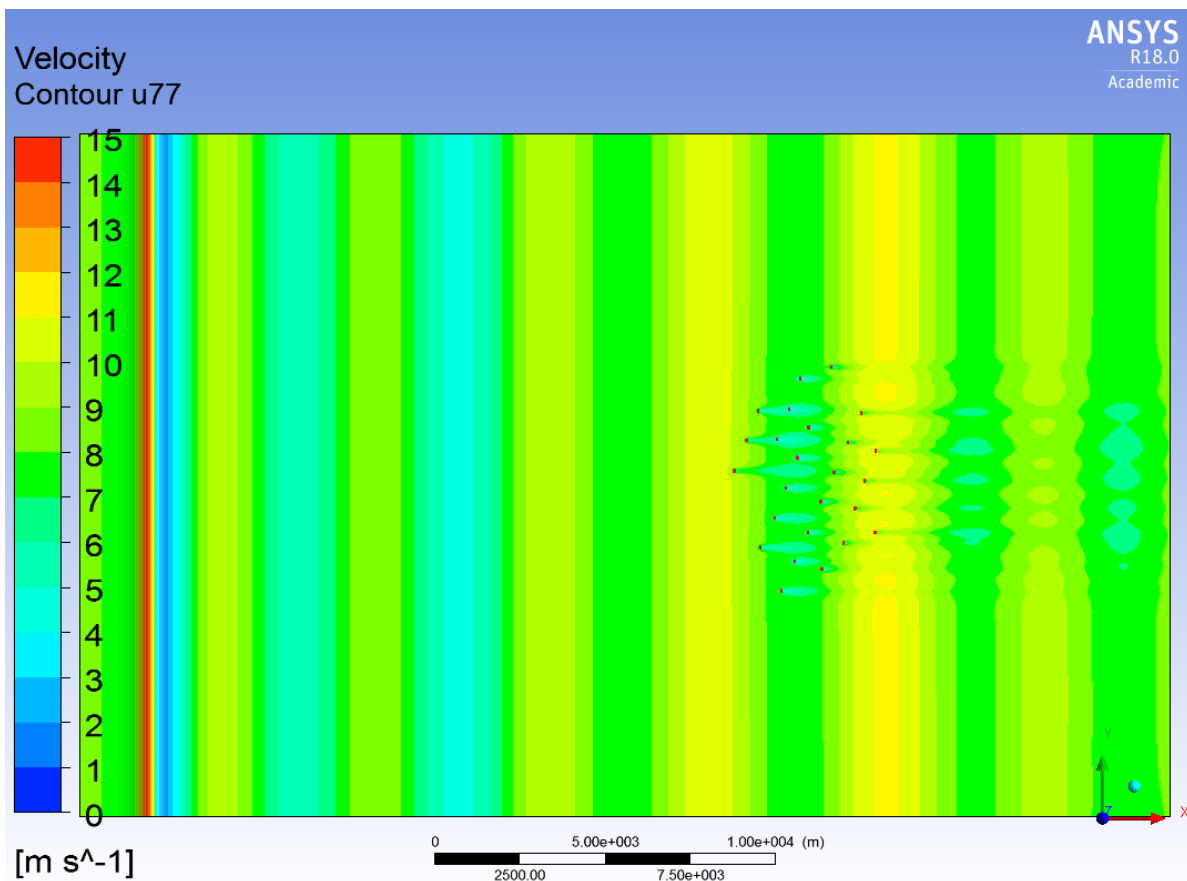
Figure 4. Hub height (77m) wind velocity for the domain. Red dots show the location of the turbines. Legend shows the key for wind velocity.
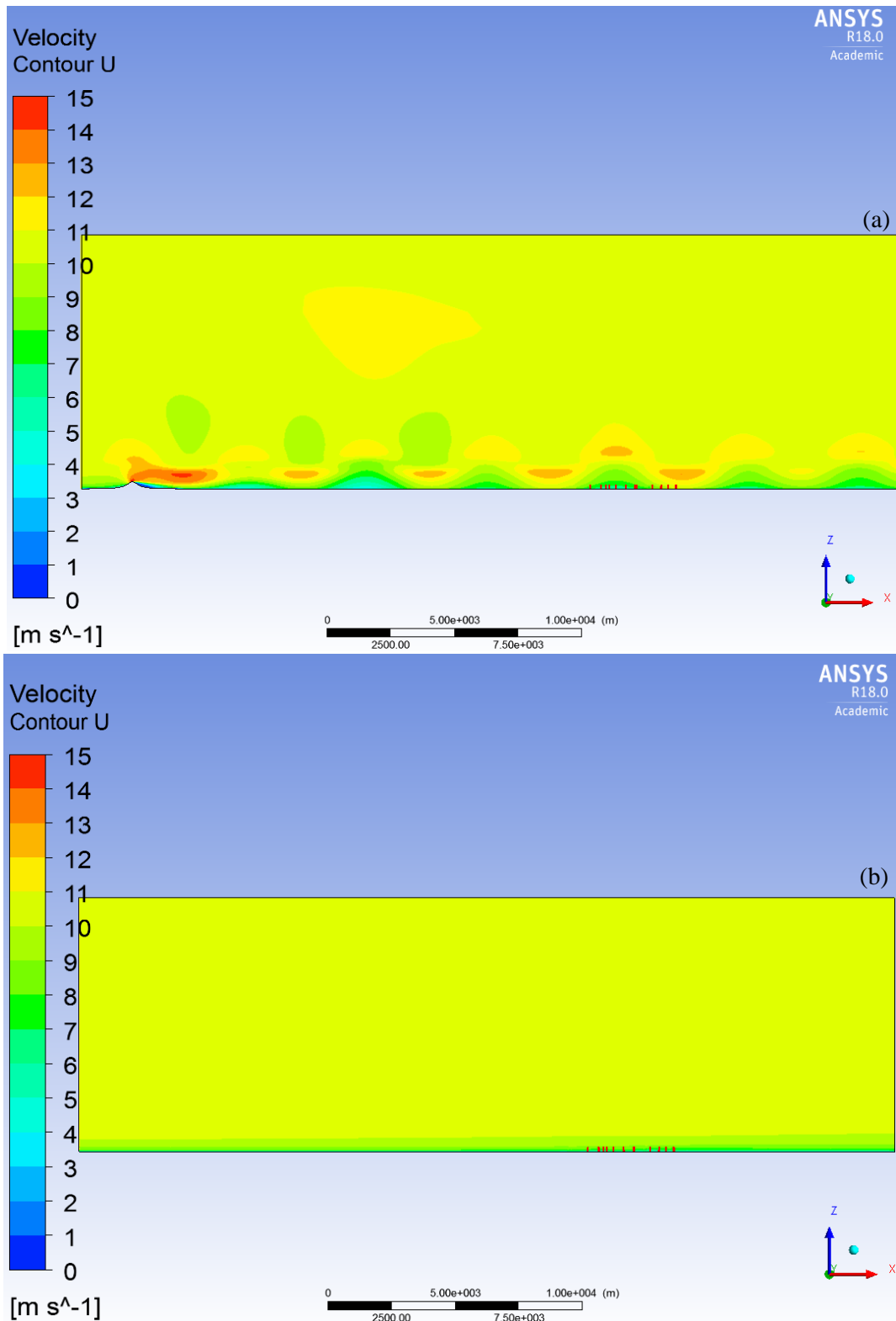
Figure 5. (a) AGW case - Vertical slice through the centre of the domain showing velocity. Legend shows the key for wind velocity. (b) Control case.
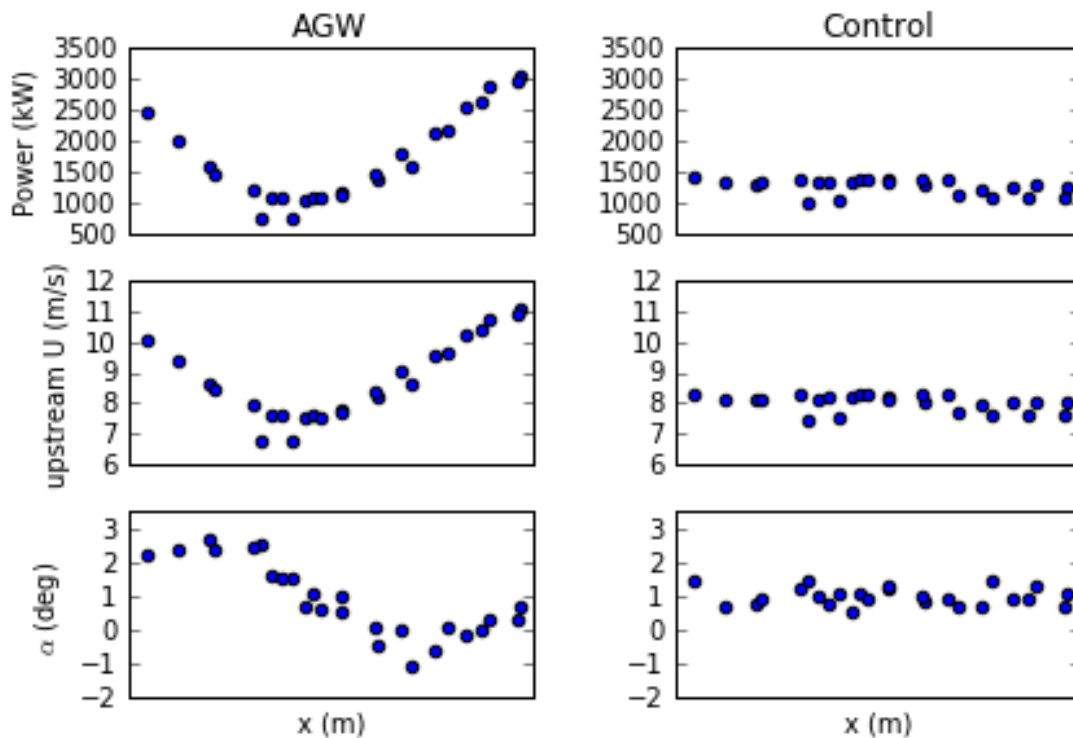
Figure 6. Power, upstream windspeed (U) and upflow angle (α) for the turbines along the x direction in the domain for AGW case (left hand side) and control (right hand side).

4.Discussion and Preliminary Conclusions

The preliminary results demonstrate that AGWs can have a substantial impact on the variation in wind speeds experienced across an offshore wind farm and the resulting power output potential of individual wind turbines within the wind farm. In this example, the reference wind speed at the inlet is analogous to a mast measurement taken 20km upstream of a proposed wind farm site. Despite the top of the ridge being 20km upstream of the farm (5km inland from the coast), its influence is detected at the turbines and this is enhanced by the effect of an upper layer inversion to force strong AGWs. These results demonstrate that with the same apparent synoptic forcing conditions, local conditions favouring AGW formation may lead to large deviations between the predicted and actual wind speed. Thus, power output from individual turbines and whole farms will vary significantly from predicted if these conditions are not accounted for.

Whilst this preliminary research shows the potential perturbation to wind power, the magnitude of the perturbation will be sensitive to many variables, for example as the upstream wind speeds vary considerably throughout the AGW, the position of the windfarm in the wave cycle will strongly influence the power output. Wind farm layout and varying wake effects, the inlet wind speed and direction, surface atmospheric stability, inversion strength, inversion height and depth and topography dimensions and orientation will all also have considerable influence on the overall AGW impact. Thus, subsequent investigations will aim to address these factors by altering these parameters within the AGW domain. The impact of the AGWs will also be considered regarding changes to the local wind shear and upflow angle at locations in the offshore wind farm which will have an impact on turbine loading and potential fatigue lifetime. Furthermore, it is important to consider the prevalence and impact of AGWs when assessing the operational outputs of wind farms where such phenomena are likely to occur. Thus, future work will develop an AGW climatology for UK wind farms.

Importantly, whilst these results relate to AGW influences on an offshore wind farm, where AGW form over onshore windfarms the perturbation to power output associated with AGW is also expected. For example, AGW influences are expected to be important for wind farms downstream of mountain ranges such as those in the Great Plains, USA. These farms have conditions favourable for AGW formation due to their siting on flat topography in lee of topographical obstacles, leading to stable boundary layer formation [18] similar to those presented here.

Also, whilst we discuss an AGW in the lee of a topographical obstacle, near surface AGW of any origin are likely to cause similar perturbation to energy outputs. Finally, AGWs are not just UK-based phenomena but are present worldwide where the conditions are favorable, so an understanding of these impacts may be important for the wind industry worldwide.

5.References

[1]   Gossard E E and Hooke W H 1977 *Waves in the Atmosphere* (Elsevier Scientific Publishing)

[2]   Rasmussen E A and Aakjær P D 1992 Two Polar Lows Affecting Denmark *Weather* **47** 326–38

[3]   Romanova N N and Yakushkin I G 1995 Internal gravity waves in the lower atmosphere and sources of their generation (review) *Ocean. Phys. C/C* **31** 151–72

[4]   Chunchuzov I, Vachon P W and Li X 2000 Analysis and Modeling of Atmospheric Gravity Waves Observed in RADARSAT SAR Images *Remote Sens. Environ.* **74** 343–61

[5]   Nappo C J 2012 Gravity waves in stable atmospheric boundary layers *Workshop on Workshop on Diurnal cycles and the stable boundary layer, 7-10 November 2011* (Shinfield Park, Reading: ECMWF) pp 55–61

[6]   Allaerts D and Meyers J 2017 Boundary-layer development and gravity waves in conventionally neutral wind farms *J. Fluid Mech.* **814** 95–130

[7]   Thomson R E, Vachon P W and Borstad G A 1992 Airborne synthetic aperture radar imagery of atmospheric gravity waves *J. Geophys. Res. Ocean.* **97** 14249–57

[8]   Vachon P W, Johannessen O M and Johannessen J A 1994 An ERS 1 synthetic aperture radar image of atmospheric lee waves *J. Geophys. Res. Ocean.* **99** 22483–90

[9]   Smith R B 2010 Gravity wave effects on wind farm efficiency *Wind Energy* **13** 449–58

[10]   Wu K, Porté-agel F, 2017 Flow Adjustment Inside and Around Large Finite-Size Wind Farms *Energies* **10** 2164.

[11]   Allaerts D and Meyers J 2018 Gravity Waves and Wind-Farm Efficiency in Neutral and Stable Conditions *Boundary-Layer Meteorol.* **166** 269-299**.**

[12]   Montavon C and Jones I 2009 Practical Issues in the Use of CFD for Modelling Wind Farms *European Wind Energy Conference* (Marseille)

[13]   Siemens AG 2011 New dimensions Siemens Wind Turbine: SWT-3.6-107

[14]   Garratt J R 1994 Appendix 3 *The atmospheric boundary layer* (Cambridge atmospheric and space science series. Cambridge University Press)

[15]   Montavon C, Jones I and Wells A K 2012 *D3 Final Report: Modelling Offshore Wind Farms using CFD, Carbon Trust Report, OWA Phase II*

[16]   ANSYS 2017 *ANSYS CFX Solver Theory Guidem Version 18.0*

[17]   Montavon C and Jones I 2013 Atmospheric stability and Coriolis effects in the simulation of large array losses *EWEA* (Vienna)

[18]   Bonin T A, Blumberg W G, Klein P M and Chilson P B 2015 Thermodynamic and Turbulence Characteristics of the Southern Great Plains Nocturnal Boundary Layer Under Differing Turbulent Regimes *Boundary-Layer Meteorol.* **157** 401–20